



In-vitro perforation of the round window membrane via direct 3-D printed microneedles

Aykut Aksit¹ · Daniel N. Arteaga² · Miguel Arriaga¹ · Xun Wang¹ · Hirobumi Watanabe¹ · Karen E. Kasza¹ · Anil K. Lalwani^{1,2} · Jeffrey W. Kysar^{1,2}

Published online: 8 June 2018
© Springer Science+Business Media, LLC, part of Springer Nature 2018

Abstract

The cochlea, or inner ear, is a space fully enclosed within the temporal bone of the skull, except for two membrane-covered portals connecting it to the middle ear space. One of these portals is the round window, which is covered by the Round Window Membrane (RWM). A longstanding clinical goal is to reliably and precisely deliver therapeutics into the cochlea to treat a plethora of auditory and vestibular disorders. Standard of care for several difficult-to-treat diseases calls for injection of a therapeutic substance through the tympanic membrane into the middle ear space, after which a portion of the substance diffuses across the RWM into the cochlea. The efficacy of this technique is limited by an inconsistent rate of molecular transport across the RWM. A solution to this problem involves the introduction of one or more microscopic perforations through the RWM to enhance the rate and reliability of diffusive transport. This paper reports the use of direct 3D printing via Two-Photon Polymerization (2PP) lithography to fabricate ultra-sharp polymer microneedles specifically designed to perforate the RWM. The microneedle has tip radius of 500 nm and shank radius of 50 μm , and perforates the guinea pig RWM with a mean force of 1.19 mN. The resulting perforations performed *in vitro* are lens-shaped with major axis equal to the microneedle shank diameter and minor axis about 25% of the major axis, with mean area 1670 μm^2 . The major axis is aligned with the direction of the connective fibers within the RWM. The fibers were separated along their axes without ripping or tearing of the RWM suggesting the main failure mechanism to be fiber-to-fiber decohesion. The small perforation area along with fiber-to-fiber decohesion are promising indicators that the perforations would heal readily following *in vivo* experiments. These results establish a foundation for the use of Two-Photon Polymerization lithography as a means to fabricate microneedles to perforate the RWM and other similar membranes.

Keywords Inner ear delivery · Round window membrane · 3-D laser printing · Microneedles · Nanoscribe

1 Introduction

An estimated 500 million people worldwide suffer from auditory and vestibular dysfunctions (Stevens et al. 2013).

Karen E. Kasza, Anil K. Lalwani and Jeffrey W. Kysar are Senior Authors.

Hirobumi Watanabe is currently at Kernel.

✉ Jeffrey W. Kysar
jk2079@columbia.edu

¹ Department of Mechanical Engineering, Columbia University, 220 Mudd Building 500 West 120th Street, New York, NY 10027, USA

² Department of Otolaryngology - Head, Neck Surgery, Columbia University College of Physicians and Surgeons, New York, NY 10032, USA

The underlying causes of many hearing disorders such as sudden or progressive sensorineural hearing loss (SNHL) and tinnitus as well as vestibular disorders such as Ménière's disease manifest themselves within the cochlea (or inner ear). The cochlea is a fluid-filled cavity within the temporal bone of the skull, which is one of the hardest bones in the body. One of the main challenges in treating such auditory and vestibular disorders is the anatomic inaccessibility of the cochlea, which makes it extremely difficult to deliver therapeutics into it (McCall et al. 2010). The development of reliable methods for the precise delivery of therapeutics — including pharmaceutical, molecular and cellular agents — to the inner ear while preserving hearing function and maintaining cochlear architecture remains a formidable challenge in the field of Otology, and is the focus of this study.

Current state-of-the-art treatments intended to deliver therapeutics into cochlea are limited to intratympanic

injection of the therapeutic into the middle ear space, after which some of the therapeutic material diffuses across the round window membrane (RWM) into the cochlea. The efficacy of this technique is limited by the unpredictable rate of molecular transport across the RWM. Other methods of direct delivery of therapeutic agents into the cochlea exist, but these techniques breach the inner ear and risk hearing impairment from surgical manipulation and traumatic disruption of the cochlea (Liu et al. 2013). Thus, a safe and reliable method for direct and precise intracochlear delivery remains to be developed.

Despite these challenges, the RWM shows promise as a portal for intracochlear delivery. A thin physical membrane that protects the cochlea from middle ear pathology, the RWM displays absorptive capabilities and allows permeation of a large range of materials, including various antimicrobials, steroids and macromolecules (Goycoolea and Lundman 1997). RWM permeability, however, is selective and affected by size, charge, liposolubility and morphology of the compound, as well as RWM thickness (Goycoolea and Lundman 1997; Goycoolea et al. 1988). Moreover, the experimental diffusion rate of individual therapeutic reagents across the RWM varies widely from animal to animal, demonstrating a critical need for tools that reduce the variability in molecular transport into the cochlea (Hahn et al. 2006; Plontke et al. 2007).

Introducing microscopic perforations across the RWM with the goal of enhancing the membrane's permeability to therapeutic materials may help overcome these challenges. Microneedle arrays—extensively studied for rapid and painless administration of drugs across the dermis—could safely and reliably reduce the natural variability in the rate of molecular transport across the RWM (Faraji Rad et al. 2017; Yu et al. 2015). Previously, our laboratory has demonstrated that microscopic perforations allow for predictable diffusion of materials across the RWM of guinea pigs *in vitro* (Kelso et al. 2015). Ultimately, the use of such microneedles may lead to improvements in intratympanic injection delivery that could be accomplished during an office visit.

The objective of this paper is to report a new method for the fabrication of microneedles that can be used to introduce microperforations across the RWM. The fabrication method employs direct 3D-printing via two-photon lithography to manufacture ultra-sharp microneedles specifically designed to perforate the RWM. We measure the force that must be exerted on the needle to perforate the RWM. We also employ confocal microscopy to characterize the size and shape of the perforations introduced by the microneedles. Our results demonstrate that needles fabricated in this method have sufficient sharpness and strength to introduce micro-scale perforations across

the RWM without causing the RWM to rip or otherwise tear.

2 Microneedle fabrication methods

A variety of production methods, including micromachining and direct writing techniques, allow for the manufacturing of needles with micro-scale features geared toward drug delivery (Donnelly et al. 2010; Park et al. 2006; Larrañeta et al. 2016). This section introduces the principles of needle fabrication by the following techniques: Micromachining, Electric Discharge Machining (EDM), Selective Laser Sintering (SLS), Stereolithography (SLA) and Two-Photon Polymerization (2PP).

Originally developed for use in the semiconductor and microelectromechanical systems (MEMS) industries, multiple micromachining techniques have been successfully utilized in the making of microscopic needles. These methods include isotropic or anisotropic etching of silicon with a photoresist or oxide pattern, etching of glass, and patterning of SU-8 (Han et al. 2009; Donnelly et al. 2010; Izumi and Aoyagi 2007; Henry et al. 1998; Lin and Pisano 1999). While these methods are highly optimized, inexpensive and readily scalable, they are ultimately limited as they offer little process control and design freedom to engineers utilizing the technology.

Wire Electric Discharge Machine (EDM) uses an electrically charged single-strand of metal wire to machine a metal substrate. When the charged wire approaches the metal substrate, an electrical spark is generated and the resulting process erodes material from the substrate. This method has been used to manufacture micro-scale needles that are sufficiently durable to penetrate human tissue (Stevens et al. 2016). However, needles fabricated via EDM have sub-optimal surface finish and tip sharpness, a limitation that affects most top-down machining methods (Bleys et al. 2006).

Several direct writing processes have been used to create microscopic needles, all of which use lasers to energize a material and induce reactions that promote binding of the material. Selective Laser Sintering (SLS) uses lasers to heat a metal powder until it melts and re-solidifies into a cohesive durable material (Kruth et al. 2005). The process starts with a single layer of heat-reactive powder. After the laser finishes tracing the desired pattern on one layer, a new layer of fresh powder is supplied on top of the previously written pattern, the table adjusts its height, and the process is repeated until the sample is complete. The method is limited by the materials it can use, chemical reactions that take place at high temperatures such as oxidation, and the quality of the surface that is created (Gittard and

Narayan 2010). Similarly, Stereolithography (SLA) utilizes ultraviolet (UV) light to crosslink a photosensitive resin (Venuvinod and Ma 2004). To begin, a UV laser traces the desired pattern upon the surface of a non-reactive substrate. After the patterning is complete, a fresh layer of resist is placed on the previously written pattern, and the process is repeated until completion of the desired structure. Commercially available SLA type printers do not have sufficient resolution to generate feature sizes in the range that is necessary for microneedles.

The method of choice for our research is 3D direct writing with two-photon polymerization (2PP), a process by which the near-simultaneous absorption of two photons excites and crosslinks a photosensitive resin to generate a durable polymer. As in SLA, a viscous resin—typically a synthetic substance containing acrylate, epoxy, urethane acrylate or vinyl ether functional groups—is placed on a non-reactive substrate. Ultrashort and tightly focused laser pulses are then used to trigger polymerization in an individual voxel of the region to be printed. The focal point then traces the desired pattern voxel-by-voxel until a complex 3-D structure emerges (Serbin et al. 2003). The nonlinearity of two-photon absorption causes crosslinking of the material to occur within a voxel smaller than the diffraction limit, resulting in superior resolution approaching the scale of 100 nm. The lasers used in 2PP utilize microscope objectives, thus allowing for easy selection of voxel size of the desired scale. Combining the precision of microtechnology and the design freedom of regular 3D printing, 2PP is the ideal candidate for fabricating polymeric microneedles (Suzuki et al. 2015). In this communication, we report on the use of micro-scale 3-D printing to create microneedles optimized for RWM perforation.

3 Methods

3.1 Microneedle fabrication

We employed single crystal Si (100) wafers as the substrate material for 2PP laser writing due to its low price and commercially-available highly polished surface. The Si wafers were cut into 25×25 mm square slides followed by Piranha cleaning and rinsing with acetone and isopropyl alcohol (IPA) to ensure a clean surface.

The 2PP 3D laser writing was performed using the Photonic Professional GT system (Nanoscribe GmbH, Karlsruhe, Germany). The photoresist employed was IP-S (Nanoscribe GmbH, Karlsruhe, Germany) in a Dip-in Laser Lithography (DiLL) configuration with a $25\times$ objective (Nanoscribe GmbH, Karlsruhe, Germany). Stereolithography (STL) files were generated using the SolidWorks (Dassault Systems SolidWorks Corporation, Concord, NH, USA)

computer aided design (CAD) software. These subsequently were converted into Direct Laser Writing commands via the Describe (Nanoscribe GmbH, Karlsruhe, Germany) software.

The proprietary IP-S photoresist was drop cast onto the substrate, and the microscope objective was immersed into the photoresist. The 2PP writing started at the out-of-plane z-position of $1 \mu\text{m}$ within the substrate to ensure good anchoring as well as to account for possible slight tilting of the substrate. Other writing parameters such as writing speed ($40000 \mu\text{m/s}$), laser intensity (35% at interface, 100% at scaffolds and 100% at contours), hatching distance ($0.75 \mu\text{m}$) were also specified after multiple trials. The stage was mobilized using the piezo-motor and the laser was used to scan the field of view of the objective using galvo-scan mode. Since the field of vision of the laser is not wide enough to write the entire structure, the structure to be written was divided into hexagonal regions with the major axis set at $350 \mu\text{m}$, and the stage was used to move between these regions and write them separately, leaving an overlap of μm for good stitching.

After 2PP writing was complete, the samples were put into a propylene glycol monomethyl ether acetate (PGMEA) solution for 20 minutes, and were subsequently cleaned in two IPA baths of length 35 minutes and 25 minutes. The extended IPA baths were necessary to remove uncured photoresist from an annular cavity in the base of the needle, which will be discussed in the next section. Nanoscribe GmbH (Karlsruhe, Germany) (Nanoscribe GmbH 2018) reports that the resulting polymer has mechanical properties with approximate values: Young's modulus of 4.5 GPa, hardness of 160 MPa, storage modulus of 5 GPa, and loss modulus of 150–350 MPa. All data were acquired with a G200 Nanoindenter. The specimen from which Young's modulus and hardness were measured was a $100 \times 100 \times 100 \mu\text{m}^3$ solid block written with the 25×0.8 objective using the following parameters: slicing: $1 \mu\text{m}$; hatching $0.5 \mu\text{m}$. The specimen from which storage and loss moduli were acquired was cylindrical with a $10 \mu\text{m}$ diameter at a temperature of 26°C .

3.2 Microneedle design and fabrication

In this study we design and fabricate microneedles to perforate the RWM of a guinea pig (GP), which has a thickness of approximately $10 - 30 \mu\text{m}$ (Mittmann et al. 2014; Tanaka and Motomura 1981). Figure 1 shows the final microneedle design. For simplicity, we designed a solid cylindrical needle with a constant shank radius of $50 \mu\text{m}$ and height $200 \mu\text{m}$ with a subsequent 9° taper to the needle tip. The very small voxel size attainable with 2PP printing allows ultra sharp needles to be printed. Here we define the “sharpness” of a needle as the radius of curvature of its tip. In order

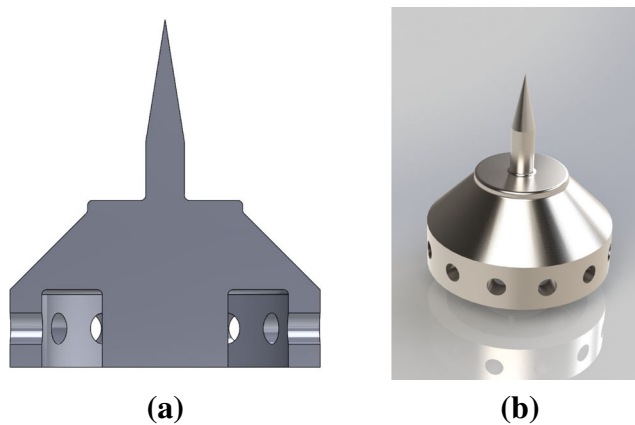


Fig. 1 Microneedle design: **(a)** Cross-sectional image of microneedle design and its base. Fillets can be seen at the base of the needle shaft to reduce possible stress concentrations due to bending. The base of the needle can be seen to have the imprint of a Gage 23 Blunt Tip Needle; **(b)** 3D graphical rendering of the design

to perforate a membrane efficiently, the radius of curvature of the microneedle tip must be much less than the thickness of the membrane. In this study, we specify the needle radius of curvature to be 500 nm. Figure 1a shows a center cross-section of the microneedle with associated base.

The base of the needle was designed with practicality in mind. One shortcoming of structures made using micro-fabrication methods is the difficulty of readily mounting them to tools easily utilizable by clinicians. In the present study, this challenge was overcome by designing the base of the microneedle structure to be mounted directly onto a commercially available Gage 23 syringe tip (industrial

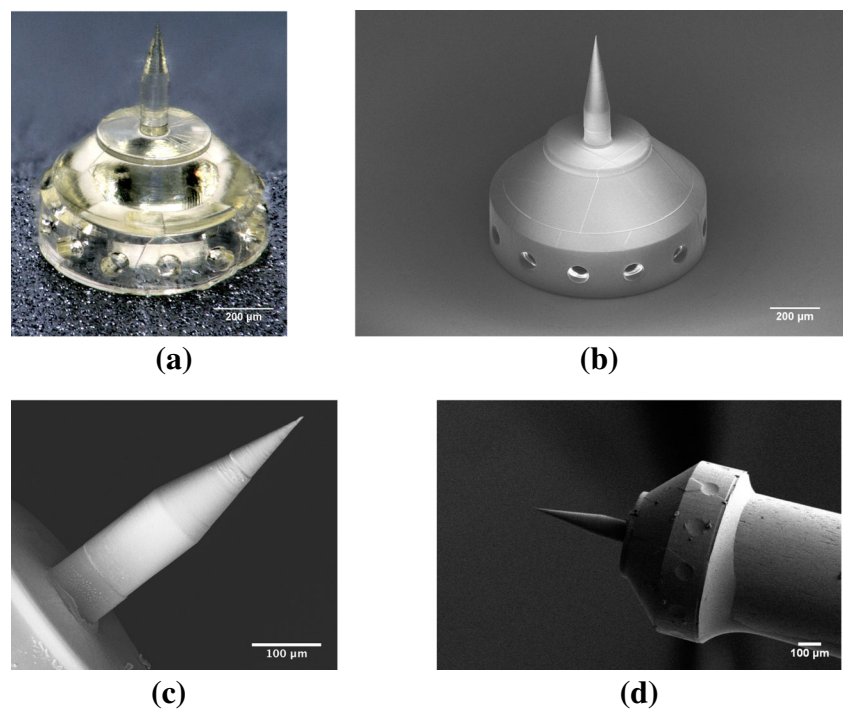
unsterilized Blunt Tip Dispensing Needle with Luer Lock) of length 12.7 mm, inside radius of 170 μm and outside radius of 320 μm . An annular cavity in the base serves to mate the base to the blunt dispensing needle. To reduce printing time, the base of the needle was designed to be partially hollow. In order to allow a pathway for the uncured IP-S photoresist within the base to exit, small holes were incorporated into the interior surface of the annular cavity. A 3D rendering of the design is shown in Fig. 1b.

Figure 2 shows examples of the printed microneedles. Figure 2a is an optical microscope image of the microneedle and base, and Fig. 2b shows the same needle in an SEM (Zeiss, Oberkochen, Germany). Figure 2c shows a SEM micrograph of a printed microneedle. Figure 2d shows the microneedle and base mounted on a Gage 23 blunt syringe tip and secured by resin epoxy. Finally, Fig. 3 shows a high-magnification SEM micrograph of the microneedle tip, which confirms the tip radius to be 500 nm or smaller. The precision of the individual voxels are smaller than the wavelength of visible light, so the microneedle surface is specularly reflective at visible wavelengths.

3.3 Harvesting guinea pig cochleae

Carcasses of mature guinea pigs (Hartley, Charles River, Massachusetts) with no history of middle ear disease were obtained via tissue sharing facilitated by the Institute of Comparative Medicine at Columbia University Medical Center. All animals were euthanized using pentobarbital overdose for the purpose of harvesting their trachea.

Fig. 2 Images of a microneedle printed via two-photon lithography: **a** Optical microscope image of a polymer microneedle and base; **b** SEM image of microneedle and base; **c** SEM image of a microneedle; **d** SEM image of a microneedle and base mounted on the end of a blunt 23 Gage syringe tip and secured by epoxy resin glue



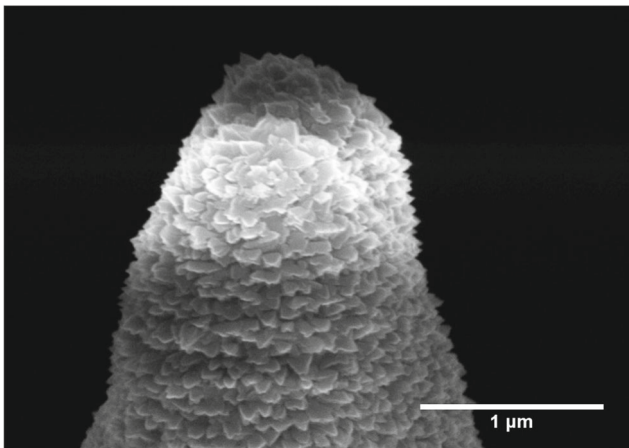


Fig. 3 SEM Image of a microneedle tip coated with sputtered titanium for characterizing tip geometry. The surface roughness has a length scale of about 100 nm, which coincides with the precision easily obtainable in 2PP lithography processes

Immediately following euthanasia, the intact temporal bone of the guinea pig was harvested using blunt dissection. An Osada Electric Handpiece System (Osada, Inc., Los Angeles, California, USA) was used to drill and remove the surrounding bone, exposing a clear, wide-angle view of the RWM. The resulting specimen was rinsed with 0.9% saline solution and inspected for gross membrane perforations and fractures of the RWM niche. If perforation of the RWM with the microneedles could not be performed immediately, the specimen was refrigerated in 0.9% saline solution (up to a maximum of 24 hours) prior to further experimental use. During perforation experiments, small amounts of sterile 0.9% saline solution were applied at regular intervals to keep the membrane from drying.

3.4 Instrumented indentation of cochlea with microneedle

A microindenter setup was built in-house for repeatable controlled perforations of the harvested RWM. The system measures the force vs. displacement response during indentation. It consists of the following components:

- Motorized stage for moving harvested RWM into position (Zaber Technologies Inc., Vancouver, British Columbia, Canada)
- Motorized linear translator onto which the indenter needle is mounted (Zaber Technologies Inc., Vancouver, British Columbia, Canada)
- Force transducer with full scale of 10 grams-force for measurement of axial force exerted on needle during indentation (Transducer Techniques, Temecula, California, USA).

The indentation experiment was conducted with a constant needle speed of $5 \mu\text{m/s}$. Imaging during *in vitro*

experimentation was made using a 3D digital microscope (VHX-5000, Keyence Corporation of America, Elmwood Park, NJ, USA). The images and videos acquired via the digital microscope were used to position the RWM in relation to the microneedle, as well as to verify positions of perforations, in conjunction with the force data acquired during perforation. Figure 4 shows an image of the microneedle during the indentation process.

3.5 Confocal microscopy of perforated membranes

After perforation and prior to imaging, the RWM was immersed in a 1 mM solution of Rhodamine B in phosphate buffered saline (PBS) for 1 hour. It was then rinsed several times with PBS and placed in a MatTek glass bottom dish (No. 1.5). The imaging of the perforated membrane was done on an inverted confocal laser scanning microscope Zeiss LSM 880, Axio Observer with a $10\times$ objective (EC Plan-Neofluar $10\times/0.30$ M27) or a $20\times$ objective (Plan-Apochromat $20\times/0.8$ M27). An excitation wavelength of 561 nm was chosen for the laser, and emitted light from 576 nm to 682 nm was allowed to pass to the detector. A stack of images was generated at several focal heights spaced $1 \mu\text{m}$ and $5 \mu\text{m}$ apart for the $20\times$ objective and the $10\times$ objective, respectively. These images were then projected in the stacking direction (maximum intensity z-projection) to obtain a global image with the visible perforation.

4 Results

4.1 Perforation force data

We first consider the force on the microneedle necessary to perforate the RWM at a constant velocity, in this case

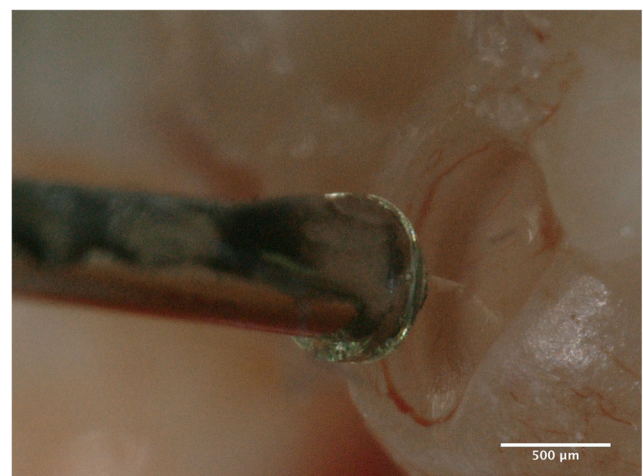


Fig. 4 Image of a microneedle attached to the microindenter - force transducer setup in contact with a harvested Guinea Pig RWM taken with a digital microscope

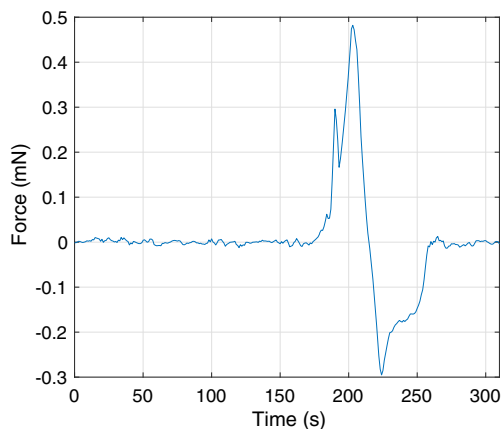


Fig. 5 Force vs. time response of representative perforation experiment. Contact of the microneedle tip with the RWM occurs around $t = 175$ s. The recorded indentation force is 0.29 mN, when $t = 190$ s, at which time the needle tip initially perforates the RWM. The force then increases again as the tapered portion of the needle enlarges the perforation with further displacement through the RWM. The entirety of the tapered section of the needle passes through the membrane after $t = 200$ s, and is retracted upon visual confirmation of the event. The force necessary for further perforation decreases because the perforation has reached its maximum size. As the needle travels back, from $t = 215$ s to $t = 260$ s, a negative force is seen to act on the needle. This is due to the friction between the membrane and the needle

5 $\mu\text{m/s}$. A representative plot of force vs. time in Fig. 5 shows a local maximum and a global maximum in force. We interpret the initial local maximum to be the force at which the microneedle tip “pops” through the RWM to make an initial perforation. The size of this initial perforation scales with the microneedle tip radius rather than the shank radius. Therefore, the microneedle must enlarge the perforation by continuing to move through the RWM until the shank fully perforates it, which occurs at the global maximum in force. In all cases, we report the global maximum as the “Perforation Force.” We will investigate in future studies the details of the initial perforation event and how that depends upon tip radius as well as the angle of the taper.

The local maximum force at initiation of the perforation is important for the detailed design of the needle tip. The force vs. time plot for some of the perforations did not exhibit the initial local maximum, which may indicate that the microneedle tip does not “pop” through the RWM. In this case we expect the perforation process to be continuous. The global maximum depends upon the microneedle shank radius and to a lesser extent on the velocity of penetration as a consequence of viscoelastic behavior in the RWM. The value of this global maximum is an important design consideration for the overall size and shape of the microneedle.

Figure 6 shows the distribution of the perforation force data, with a mean perforation force of 1.19 mN and a standard deviation of 0.61 mN. With our data of $n = 9$, we have

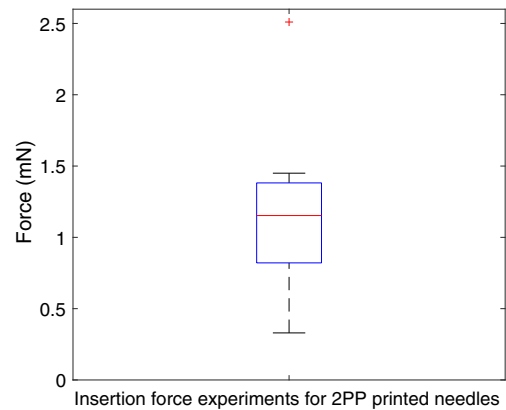


Fig. 6 Box plot for measured perforation forces. The bottom and top edges of blue box indicate the 25th and 75th percentiles, respectively. The mean value is halfway between the 25th and 75th percentiles. The horizontal red central mark indicates the median. The vertical whiskers extend to the most extreme data points not considered outliers, and outliers are plotted individually using the ‘+’ symbol

executed a single tailed t-test and observed with a 95% confidence level that the mean perforation force for the manufactured needles is less than 1.6 mN, for Guinea Pig Round Window Membranes with the produced microneedles.

4.2 Analysis of perforations with confocal microscopy

The shape and area of the perforations created with the microneedles were studied by imaging the RWM with a confocal microscope. Figure 7 shows an approximate plan view of an RWM with a perforation roughly in its center. The perforation is lens-shaped and remains partially open after the microneedle is removed. The non-circular shape of the perforation indicates anisotropy of the microstructure and mechanical properties of the RWM, consistent with our previous studies with a non-circular microneedle (Stevens et al. 2016).

Figure 8 shows a higher magnification image of the membrane in the region that contains the perforation. The length of the residual opening in the major axis has a mean of 95.9 μm and a standard deviation of 7.8 μm , which is essentially the same as the microneedle diameter of 100 μm . However, the length of the residual opening in the minor axis is only about 25% of the microneedle diameter: the measurements have a mean of 25.4 μm with a standard deviation of 6.3 μm .

Figure 9 shows a confocal microscope image at a higher magnification that resolves the various fibers of the connective tissue within the RWM tissue (Rezakhaniha et al. 2012; Yasui et al. 2004; Chen et al. 2012). The direction of the major axis of the perforation is roughly aligned with the main direction of the fibers of connective tissue.

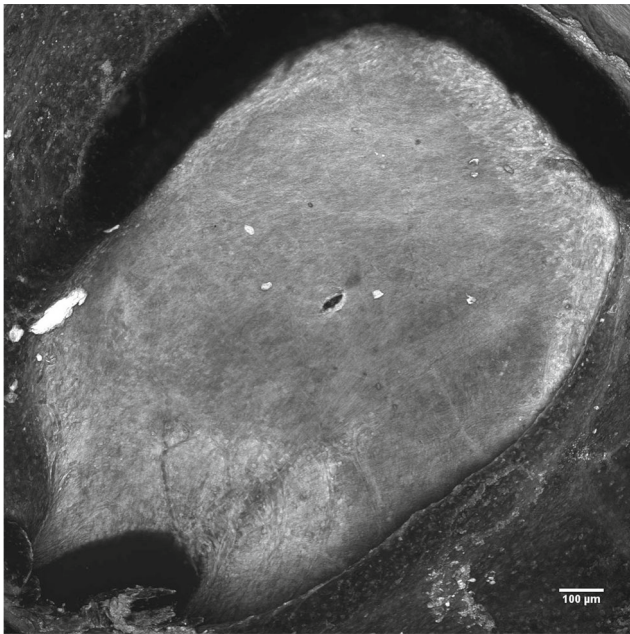


Fig. 7 Confocal image of the entire Round Window Membrane with a perforation made by a microneedle with a 50 μm radius manufactured using 2PP

Figure 10 quantifies the lengths of the major and minor axes and Fig. 11 quantifies the open perforated area. When the microneedle is inserted fully into the RWM, both the major and minor axes of the perforation must be at least the same as the shank diameter. Upon retraction of the needle

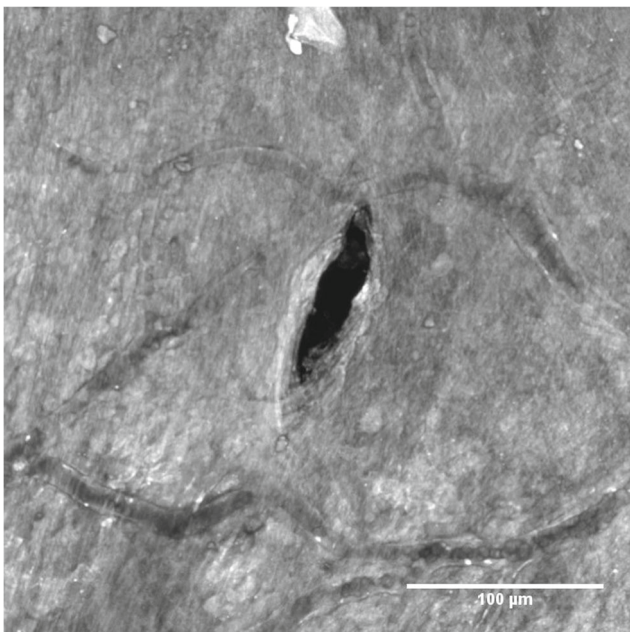


Fig. 8 Confocal image of a RWM zoomed in around a perforation made by a microneedle manufactured using 2PP. Blood vessels containing red blood cells can be seen for size comparison. Guinea pigs have red blood cells that are around 7.4 μm in diameter (Flindt 2006)

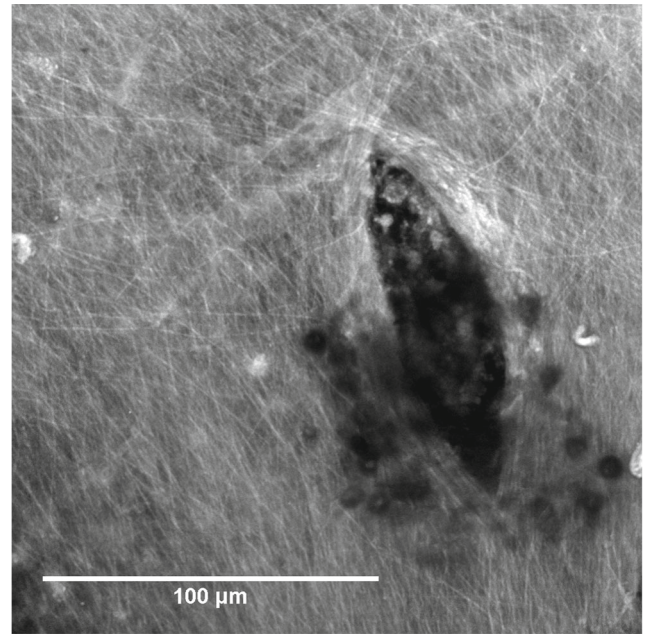


Fig. 9 Confocal image of a RWM zoomed in around a perforation made by a microneedle manufactured using 2PP. The major axis of the lens-shaped perforation is aligned with the fibers of connective tissue and fiber reorientation at the crack tip can be observed. The small dark circular features are cellular debris that is occluding the view

the opening in the direction of the minor axis decreases to about 25% of that length while the opening of the major axis does not decrease significantly if at all.

The resulting area of the holes were observed to have a mean and standard deviation of 1670 μm² and 476 μm², respectively. This area was computed digitally, and it was of interest to determine if the resulting area was similar to that of an ellipse with the identical major and minor axes. Figure 11 illustrates this comparison, and it is clear that

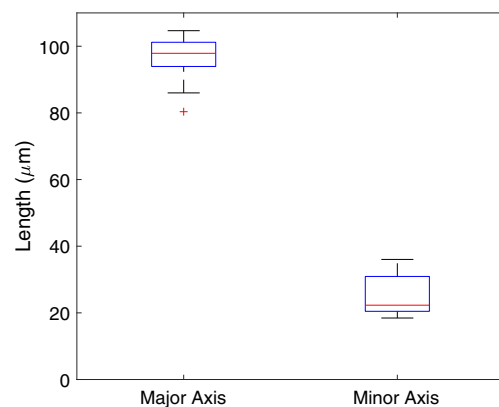


Fig. 10 Lengths of major and minor axes of perforations. The bottom and top edges of blue box indicate the 25th and 75th percentiles, respectively. The mean value is halfway between the 25th and 75th percentiles. The horizontal red central mark indicates the median. The vertical whiskers extend to the most extreme data points not considered outliers, and outliers are plotted individually using the '+' symbol

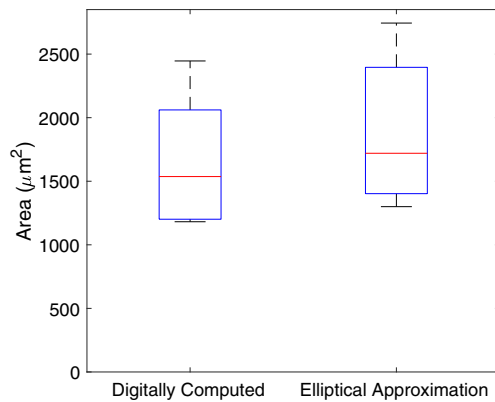


Fig. 11 Area of openings caused by perforations. The bottom and top edges of blue box indicate the 25th and 75th percentiles, respectively. The mean value is halfway between the 25th and 75th percentiles. The horizontal red central mark indicates the median. The vertical whiskers extend to the most extreme data points

estimating the area from the major and minor axes alone is not viable solution. A paired t-test shows that the elliptical approximation—due to the nature of the shape of the edges of our perforations—does overestimate the actual area with a significance level of 95%.

5 Discussion

The long term goal of the research described herein is to demonstrate that microperforations in the RWM can enhance the accuracy and precision of therapeutic transport into the cochlea via intratympanic injection into the middle ear space followed by diffusion across the RWM into the cochlea. In this paper we focus on a novel fabrication method of microneedles used to perforate the RWM and report on the force necessary for perforation as well as the size and shape of the resulting perforations. The shape and area of perforations are of interest because they will play a significant role in determining the rate at which therapeutics diffuse across a perforated RWM. In this section we discuss the implications of our results on design of the needles.

The RWM is in a state of tensile prestress prior to perforation (Stevens et al. 2016). As a consequence, there exists a critical threshold size of perforation below which a stable perforation can be introduced and above which the perforation will propagate unstably into a tear or rip. We do not know the critical size because the magnitude of the prestress has not been quantified. However clearly the critical size exceeds $100\ \mu\text{m}$ in guinea pig RWMs because we have successfully introduced stable perforations of that size.

The size of a RWM perforation is determined by the size of the microneedle shank. Small RWM perforations are

desirable for several reasons. First, while our goal is to introduce therapeutics into the cochlea, we must do so while minimizing leakage of perilymph from the scala tympani chamber of the cochlea into the middle ear space (Salt et al. 2007; Plontke et al. 2016). An outward perilymph flux will transport therapeutic material from the inner ear, preventing the medication from acting upon the cochlea. Microperforations impose a higher viscous resistance to fluid flow compared to larger perforations. As a consequence, the microperforations allow for the diffusive transport of therapeutic reagents into the cochlea while minimizing fluid flux out of the cochlea. Second, when the perforation in the RWM is smaller, the perforation will remain patent for a shorter amount of time before healing, and it will undergo a less prominent change in its structure (Gyo 1989). Third, a small perforation reduces the probability of transmission of infection into the cochlea due to treatment.

Needle sharpness (i.e. needle tip radius of curvature) is a crucial design and fabrication parameter to ensure safe perforation of the RWM. As needle sharpness increases, the force required for perforation decreases and the risk of trauma to the RWM reduces. Excessive application of force during surgical manipulation of the RWM risks detachment of the RWM from its sulcus (i.e. the connection to the surrounding bone). Left untreated, such an injury could result in perilymphatic fistula of the RWM, requiring surgical intervention for associated hearing and vestibular symptoms (Ga Young et al. 2012). Furthermore as the RWM undergoes perforation it is deflected into the cochlea which increases the pressure within the cochlea. This pressure jump decreases with sharper needles because the deflection into the cochlea decreases (Mittmann et al. 2014).

In the course of our perforation experiments, the microneedles, while successfully fulfilling their purpose, have been blunted. This suggests that microneedles made of polymer will be for single use only, and that stronger materials may be preferred if similar geometries need to be used in the future to reduce damage to the tip. An SEM image of a post-perforation microneedle can be seen in Fig. 12, with the tip blunted to $2.5 - 3\ \mu\text{m}$ in its radius of curvature.

Importantly, our results indicate that ultra-sharp needles with $500\ \text{nm}$ radius of curvature can perforate the RWM at extremely low forces, less than $1.6\ \text{mN}$. This low force minimizes the risk of trauma to the inner ear. Confocal examination of the RWM tissue surrounding the perforation revealed that fibers in the RWM tissue were separated along their axes without ripping or tearing of the RWM. This suggests that the main deformation mechanism to be fiber-to-fiber decohesion in the direction of the perforation major axis. That the minor axis does not close completely could be due to residual inelastic deformation induced by the needle or due to tensile prestrain in the membranes,

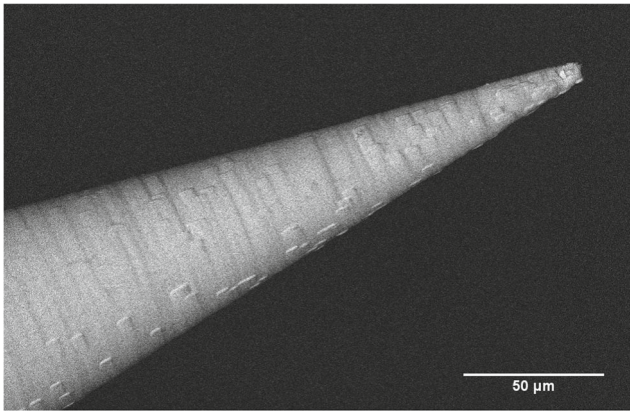


Fig. 12 An SEM image of a blunted microneedle tip after a perforation has been made on a RWM

or a combination of both. Such a growth mechanism is consistent with the notion that fibrous tissue strength is much weaker in the ground matrix perpendicular to the fibers than in the fiber directions (Von Forell et al. 2014). In addition, some fiber reorientation can be seen at the crack tip, which helps stabilize the crack against further propagation (Koh and Oyen 2015). With less sharp needles, the failure mechanism may change from a mode of fiber separation to one of fiber cutting, which would increase both trauma and the time necessary for the RWM to heal. From a manufacturing perspective, higher needle sharpness increases fabrication challenges and costs.

The shape of the RWM perforation may play a role in the delivery of therapeutics. Our results indicate that a final perforation has a major axis equal to that of the needle diameter and a minor axis approximately 25% of the needle diameter. The molecular size of the therapeutic should be much smaller than the size of the minor axis if the therapeutic is to diffuse readily through the perforation.

Thus there are several medical and technical reasons to introduce very small RWM perforations. However a small perforation area limits the quantity of therapeutic that can be delivered into the cochlea in a given time period. The overall permeability of the perforated RWM can be increased by introducing multiple microperforations simultaneously across the RWM. Figure 13 shows an array of seven microneedles that has been printed with the same methodology as described in Section 3.1.

Not only can an array of microneedles increase the total area of perforation and therefore deliver a larger therapeutic dose, it can also improve the precision of the total perforation area and therapeutic dose. For the purposes of this discussion, *accuracy* or *trueness* of a dose is defined as the difference between the mean delivered dose and the prescribed dose. The *precision* of a dose quantifies the uncertainty of the delivered dose and therefore is proportional to the standard deviation of the delivered dose (Nichols et al.

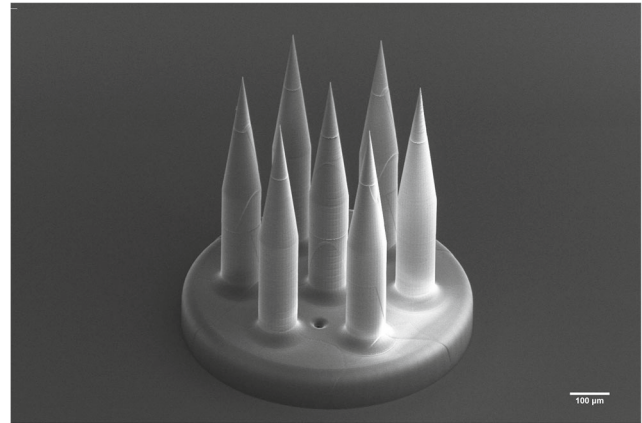


Fig. 13 SEM Image of a 7-needle microneedle array direct written via two-photon lithography, underlining the kind of design freedom provided by two-photon lithography

2014; International Organization for Standardization 1998). Strictly speaking, the precision is one-half of the width of the *confidence interval of the true mean* of the delivered dose. However since this quantity scales linearly with standard deviation, we will take standard deviation to be a proxy for precision herein. A reduction in the numerical value of standard deviation corresponds to an improvement in precision.

A single needle introducing perforations in a population of RWMs will yield perforations with mean area, μ_A , and standard deviation, σ_A . The standard deviation can be normalized by the mean area to obtain the *relative standard deviation* $\frac{\sigma_A}{\mu_A}$, which will serve as a proxy for the *relative precision*. The relative precision is convenient because it expresses the precision as a proportion or percentage of the mean value.

We now assume an array of M identical microneedles spaced sufficiently far apart so that individual perforations introduced into a population of RWMs are not affected by their neighboring perforations. Thus each of the M perforations in each RWM will have mean area, μ_A , and standard deviation, σ_A , that we will assume to be normally distributed.

It is well known that normally distributed random variables, say $X \sim N(\mu_X, \sigma_X^2)$ and $Y \sim N(\mu_Y, \sigma_Y^2)$ with mean values μ_X and μ_Y as well as standard deviations σ_X and σ_Y , respectively, have a sum $Z = X + Y$ written as $Z \sim N(\mu_X + \mu_Y, \sigma_X^2 + \sigma_Y^2)$, where the functional representation N indicates the normal distribution.

When applied to a population of RWMs perforated with an array of M microneedles, the sum of the total perforated area, A_t can be expressed as $A_t \sim N(M\mu_A, M\sigma_A^2)$. In this case, the relative standard deviation is $\frac{\sqrt{M}\sigma_A}{M\mu_A} = \frac{1}{\sqrt{M}} \frac{\sigma_A}{\mu_A}$, so the relative precision decreases in magnitude by the factor $\frac{1}{\sqrt{M}}$ as M increases. Hence the relative precision

improves by a factor of \sqrt{M} . By invoking concepts related to standard deviation of the means, we can obtain the same result even for non-normal distributions of the perforation areas.

For the case of $M = 7$ needles shown in Fig. 13, we expect the relative precision of the total area to improve by a factor of $\sqrt{7} \approx 2.65$ that of the relative precision of a single perforation. Since the diffusion rate of a sufficiently small sized therapeutic is directly related to the area available for diffusion, we expect the relative precision of the dose to improve by the same factor.

As discussed in Section 4.2, the perforations in this study have mean area of $\mu_A = 1670 \mu\text{m}^2$ and standard deviation $\sigma_A = 476 \mu\text{m}^2$, with a relative standard deviation of 0.285. If these statistics were to remain the same for an array of seven microneedles, the relative standard deviation would reduce to 0.108.

We now consider the design freedom enabled by the ease-of-use, flexibility and rapidity of 2PP and other related 3D printing fabrication methods. The needles need not be straight and need not have constant cross-sectional areas. Furthermore, the RWM surface is not planar and instead resembles a hyperbolic paraboloid (Proctor et al. 1986; Rask Andersen et al. 2004; Ghiz et al. 2001). With the 2PP process, it is possible to fabricate arrays of microneedles in which each needle has individual characteristics to account for the non-planarity of the RWM.

In this study, there are certain limitations that will be addressed in future studies. The experimental setup does not allow measurement of lateral forces on the microneedle during perforation. Such lateral forces play an important role in the potential failure mechanisms of the microneedles themselves, so it is important to quantify them under realistic conditions. In addition, the material used in this study to fabricate the microneedles is not biocompatible, therefore a coating or the usage of another material will be pursued in future studies.

6 Conclusions

We report the use of direct 3D printing via Two-Photon Polymerization (2PP) lithography to fabricate ultra-sharp polymer microneedles specifically designed to perforate the guinea pig RWM.

- The microneedle has tip radius of 500 nm and shank radius of $50 \mu\text{m}$ and perforates the guinea pig RWM with a mean force of 1.19 mN.
- The resulting perforations performed *in vitro* are lens-shaped with major axis equal to the microneedle shank diameter and minor axis about 25% of the major axis, with mean area $1670 \mu\text{m}^2$.

- The major axis is aligned with the direction of the connective fibers within the RWM; the fibers were separated along their axes without ripping or tearing of the RWM suggesting the main failure mechanism to be fiber-to-fiber decohesion.
- The small perforation area along with fiber-to-fiber decohesion are promising indicators that the perforations would heal readily following *in vivo* experiments.
- The use of arrays of microneedles has the potential to improve the precision of a therapeutic dose as compared to delivery through a single microperforation.

These results establish a foundation for the use of Two-Photon Polymerization (2PP) lithography as a means to fabricate microneedles with extremely high accuracy and resolution to perforate the RWM and other similar membranes. The sharpness of microneedles achieved by two-photon lithography would be difficult to replicate using other standard micromanufacturing techniques. Finally, the 3D printing technology allows great design flexibility of needle design with respect to sharpness, cross-sectional properties, as well as the ability to fabricate non-straight microneedles.

Acknowledgments The authors gratefully acknowledge Professor Elizabeth Olson, Charlotte PrevotEAU, Wenbin Wang, Dimitrios Fafalis, and Arnuparp Santimetaneedol for helpful discussions. Dr. Charles Emala, M.D. generously provided euthanized guinea pigs with intact temporal bones through a tissue sharing program at the Institute of Comparative Medicine at Columbia University Medical Center. KEK holds a Career Award at the Scientific Interface from the Burroughs Wellcome Fund and a Clare Boothe Luce Professorship from the Henry Luce Foundation. This work was performed in part at the Advanced Science Research Center NanoFabrication Facility of the Graduate Center at the City University of New York. This research was supported by NIH National Institute on Deafness and Other Communication Disorders of the National Institutes of Health under award number R01DC014547.

References

- P. Bleys, P. Bleys, J.P. Kruth, B. Lauwers, B. Schacht, Surface and Sub-Surface Quality of Steel after EDM. *Adv. Eng. Mater.* **8**(1-2), 15–25 (2006). <https://doi.org/10.1002/adem.200500211>
- X. Chen, O. Nadiarynkh, S. Plotnikov, P.J. Campagnola, Second harmonic generation microscopy for quantitative analysis of collagen fibrillar structure. *Nat. Protoc.* **7**(4), 654–69 (2012)
- R.F. Donnelly, T.R. Raj Singh, A.D. Woolfson, Microneedle-based drug delivery systems: microfabrication, drug delivery, and safety. *Drug Deliv.* **17**(4), 187–207 (2010)
- Z. Faraji Rad, R.E. Nordon, C.J. Anthony, L. Bilston, P.D. Prewett, J.Y. Arns, C.H. Arns, L. Zhang, G.J. Davies, High-fidelity replication of thermoplastic microneedles with open microfluidic channels. *Microsyst. Nanoengineering* **3**, 17,034 (2017)
- R. Flindt, *Amazing Numbers in Biology* (SpringerLink: Springer e-Books, Springer, Berlin, 2006)

- P. Ga Young, B. HaYoung, M. Il Joon, H. Sung Hwa, C. Yang-Sun, C. Won-Ho, Effects of early surgical exploration in suspected barotraumatic perilymph fistulas. *Clin. Exp. Otorhinolaryngol.* **5**(2), 74–80 (2012). <https://doi.org/10.3342/ceo.2012.5.2.74>
- A.F. Ghiz, A.N. Salt, J.E. DeMott, M.M. Henson, O. Henson, S.L. Gewalt, Quantitative anatomy of the round window and cochlear aqueduct in Guinea pigs. *Hear. Res.* **162**(1), 105–112 (2001). [https://doi.org/10.1016/S0378-5955\(01\)00375-6](https://doi.org/10.1016/S0378-5955(01)00375-6)
- S.D. Gittard, R.J. Narayan, Laser direct writing of micro- and nano-scale medical devices. *Expert Rev. Med. Devices* **7**(3), 343–356 (2010)
- M.V. Goycoolea, L. Lundman, Round window membrane. structure function and permeability: a review. *Microsc. Res. Tech.* **36**(3), 201–211 (1997)
- M.V. Goycoolea, D. Muchow, P. Schachern, Experimental studies on round window structure: Function and permeability. *Laryngoscope* **98**(S44), 1–20 (1988). <https://doi.org/10.1288/00005537-198806001-00002>
- K. Gyo, Healing of experimentally produced round window membrane rupture. *Acta Oto-Laryngol.* **107**(1-2), 85–89 (1989). <https://doi.org/10.3109/00016488909127483>
- H. Hahn, B. Kammerer, A. DiMauro, A.N. Salt, S.K. Plontke, Cochlear microdialysis for quantification of dexamethasone and fluorescein entry into scala tympani during round window administration. *Hear. Res.* **212**(1), 236–244 (2006). <https://doi.org/10.1016/j.heares.2005.12.001>
- M. Han, D.K. Kim, S.H. Kang, H.R. Yoon, B.Y. Kim, S.S. Lee, K.D. Kim, H.G. Lee, Improvement in antigen-delivery using fabrication of a grooves-embedded microneedle array. *Sens. Actuators B* **137**(1), 274–280 (2009). <https://doi.org/10.1016/j.snb.2008.11.017>
- S. Henry, D.V. McAllister, M.G. Allen, M.R. Prausnitz, Micromachined needles for the transdermal delivery of drugs. in *Proceedings MEMS 98. IEEE. Eleventh Annual International Workshop on Micro Electro Mechanical Systems. An Investigation of Micro Structures, Sensors, Actuators, Machines and Systems (Cat. No.98CH36176)*. <https://doi.org/10.1109/MEMSYS.1998.659807>, (1998), pp. 494–498
- International Organization for Standardization, Accuracy (Trueness and Precision) of Measurement Methods and Results — Part 5: Alternative Methods for the Determination of the Precision of a Standard Measurement Method. Standard ISO 5725-5:1998(En) International Organization for Standardization. Geneva, CH (1998)
- H. Izumi, S. Aoyagi, Novel fabrication method for long silicon microneedles with three-dimensional sharp tips and complicated shank shapes by isotropic dry etching. *IEEJ Trans. Electr. Electron. Eng.* **2**(3), 328–334 (2007). <https://doi.org/10.1002/tee.20147>
- C. Kelso, H. Watanabe, J. Wazen, T. Bucher, Microperforations Significantly Enhance Diffusion Across Round Window Membrane. *Otol. Neurotol.* **36**(4), 694–700 (2015)
- C.T. Koh, M.L. Oyen, Toughening in electrospun fibrous scaffolds. *APL Mater.* **3**(1), <https://doi.org/10.1063/1.4901450> (2015)
- J.P. Kruth, P. Mercelis, V.V. J. L. Froyen, M. Rombouts, Binding mechanisms in selective laser sintering and selective laser melting. *Rapid Prototyp. J.* **11**(1), 26–36 (2005). copyright MCB UP Limited (MCB) 2005; diagrams; illustrations; photographs; graphs; tables; references; Last update - 2014-05-21; CODEN - RPJOF
- E. Larrañeta, R.E. Lutton, A.D. Woolfson, R.F. Donnelly, Microneedle arrays as transdermal and intradermal drug delivery systems: Materials science, manufacture and commercial development. *Mater. Sci. Eng. R: Rep.* **104**, 1–32 (2016). <https://doi.org/10.1016/j.mser.2016.03.001>
- L. Lin, A.P. Pisano, Silicon-processed microneedles. *J. Microelectromech. Syst.* **8**(1), 78–84 (1999). <https://doi.org/10.1109/84.749406>
- H. Liu, J. Hao, K.S. Li, Current strategies for drug delivery to the inner ear. *Acta Pharm. Sin. B* **3**(2), 86–96 (2013). <https://doi.org/10.1016/j.apsb.2013.02.003>
- A.A. McCall, E.E.L. Swan, J.T. Borenstein, W.F. Sewell, S.G. Kujawa, M.J. McKenna, Drug Delivery for Treatment of Inner Ear Disease: Current State of Knowledge. *Ear and Hearing.* **31**(2), 156–165 (2010)
- P. Mittmann, A. Ernst, I. Todt, Intracochlear Pressure Changes due to Round Window Opening: A Model Experiment. *Sci. World J.* **2014**, 7 (2014)
- Nanoscribe GmbH, Nanoscribe GmbH. <https://www.nanoscribe.de/en/> (2018)
- T.A. Nichols, S.J. Drayton, J. Borckardt, D.J. Taber, Lithium dosing equations: Are they accurate? *Ann. Pharmacother.* **48**(5), 596–600 (2014). <https://doi.org/10.1177/1060028014524375>
- J.H. Park, M.G. Allen, M.R. Prausnitz, Polymer microneedles for controlled-release drug delivery. *Pharm. Res.* **23**(5), 1008–1019 (2006). <https://doi.org/10.1007/s11095-006-0028-9>
- P.K. Venuvinod, W. Ma, Rapid prototyping: laserbased and other technologies. Scitech Book News **28**(1), 195–244, Boston, MA: Springer US (2004). <https://doi.org/10.1007/978-1-4757-6361-4>
- S. Plontke, J. Hartsock, R. Gill, A. Salt, Intracochlear Drug Injections through the Round Window Membrane: Measures to Improve Drug Retention. *Audiol. Neurotol.* **21**(2), 72–79 (2016)
- S.K. Plontke, R. Mynatt, R.M. Gill, S. Borgmann, A.N. Salt, Concentration gradient along the scala tympani after local application of gentamicin to the round window membrane. *Laryngoscope* **117**(7), 1191–1198 (2007). <https://doi.org/10.1097/MLG.0b013e318058a06b>
- B. Proctor, B. Bollobas, J.K. Niparko, Anatomy of the round window niche. *Ann. Otol. Rhinol. Laryngol.* **95**(5), 444–446 (1986). <https://doi.org/10.1177/000348948609500502>, PMID: 3767214
- H. Rask Andersen, H. Rask-Andersen, A. Kinnefors, M. Svedberg, R.B. Illing, The human round window - A perilymph pressure regulator? On a novel mechanoreceptor-like neuron in the human round window membrane. *Audiol. Med.* **2**(3), 182–192 (2004). <https://doi.org/10.1080/16513860410018213>
- R. Rezakhaniha, A. Agianniotis, J.T.C. Schrauwen, A. Griffa, D. Sage, C.V.C. Bouten, F.N. van de Vosse, M. Unser, N. Stergiopoulos, Experimental investigation of collagen waviness and orientation in the arterial adventitia using confocal laser scanning microscopy. *Biomech. Model. Mechanobiol.* **11**(3), 461–473 (2012). <https://doi.org/10.1007/s10237-011-0325-z>
- A.N. Salt, D.B. Sirjani, J.J. Hartsock, R.M. Gill, S.K. Plontke, Marker retention in the cochlea following injections through the round window membrane. *Hear. Res.* **232**(1), 78–86 (2007). <https://doi.org/10.1016/j.heares.2007.06.010>
- J. Serbin, A. Egbert, A. Ostendorf, B.N. Chichkov, R. Houbertz, G. Domann, J. Schulz, C. Cronauer, L. Fröhlich, M. Popall, Femtosecond laser-induced two-photon polymerization of inorganic-organic hybrid materials for applications in photonics. *Opt. Lett.* **28**(5), 301–303 (2003). <https://doi.org/10.1364/OL.28.000301>
- G. Stevens, S. Flaxman, E. Brunskill, M. Mascarenhas, C.D. Mathers, M. Finucane, Global and regional hearing impairment prevalence: An analysis of 42 studies in 29 countries. *Eur. J. Public Health* **23**(1), 146–152 (2013). <https://doi.org/10.1093/eurpub/ckr176>
- J.P. Stevens, H. Watanabe, J.W. Kysar, A.K. Lalwani, Serrated needle design facilitates precise round window membrane perforation. *J. Biomed. Mater. Res. Part A* **104**(7), 1633–1637 (2016). <https://doi.org/10.1002/jbm.a.35692>
- M. Suzuki, T. Sawa, T. Takahashi, S. Aoyagi, Ultrafine three-dimensional (3d) laser lithographic fabrication of microneedle and its application to painless insertion and blood sampling inspired by

- mosquito. in *2015 IEEE/RSJ International Conference on Intelligent Robots and Systems (IROS)*. <https://doi.org/10.1109/IROS.2015.7353754>, (2015), pp. 2748–2753
- K. Tanaka, S. Motomura, Permeability of the labyrinthine windows in Guinea pigs. *Arch. Oto-Rhino-Laryngol.* **233**(1), 67–75 (1981). <https://doi.org/10.1007/BF00464276>
- G.A. Von Forell, P.S. Hyung, A.E. Bowden, Failure modes and fracture toughness in partially torn ligaments and tendons. *J. Mech. Behav. Biomed. Mater.* **35**, 77–84 (2014). <https://doi.org/10.1016/j.jmbm.2014.03.020>
- T. Yasui, Y. Tohno, T. Araki, Determination of collagen fiber orientation in human tissue by use of polarization measurement of molecular second-harmonic-generation light. *Appl. Opt.* **43**(14), 2861–2867 (2004). <https://doi.org/10.1364/AO.43.002861>
- J. Yu, Y. Zhang, Y. Ye, R. DiSanto, W. Sun, D. Ranson, F.S. Ligler, J.B. Buse, Z. Gu, Microneedle-array patches loaded with hypoxia-sensitive vesicles provide fast glucose-responsive insulin delivery. *Proceedings of the National Academy of Sciences* **112**(27), 8260–8265 (2015). <https://doi.org/10.1073/pnas.1505405112>, <http://www.pnas.org/content/112/27/8260.full.pdf>